Compressibility and crystal-fluid interactions in all-silica ferrierite at high pressure

Compressibility and crystal-fluid interactions in all-silica ferrierite at high pressure.

Paolo Lotti[1*], Rossella Arletti[2], G. Diego Gatta[1,3], Simona Quartieri[4], Giovanna Vezzalini[5], Marco Merlini[1], Vladimir Dmitriev [6], Michael Hanfland[7]

[1]Dipartimento di Scienze della Terra, Università degli Studi di Milano, Via Botticelli 23, 20133 Milano, Italy

[2]Dipartimento di Scienze della Terra, Università di Torino, Via Valperga Caluso 35, 10125 Torino, Italy

[3]CNR – Istituto di Cristallografia, Sede di Bari, Via G. Amendola 122/o, Bari, Italy

[4]Dipartimento di Fisica e Scienze della Terra, Università di Messina, Viale Ferdinando Stagno d'Alcontres 31, 98166 Messina Sant'Agata, Italy

[5]Dipartimento di Scienze Chimiche e Geologiche, Università di Modena e Reggio Emilia, Via Campi 103, 41125 Modena, Italy

[6] Swiss-Norwegian Beam Line at ESRF, BP220, 38043 Grenoble Cedex, France

[7] ESRF – European Synchrotron Radiation Facility, 71 Avenue des Martyrs, CS40220, 38043 Grenoble Cedex, France

* Correspondence author: Paolo Lotti; e-mail: paolo.lotti@unimi.it;

Tel: +390250315609; Fax: +390250315597

Abstract

The high-pressure behavior of a synthetic siliceous ferrierite has been studied by in situ single-crystal and powder synchrotron X-ray diffraction with a diamond anvil cell, using four different *P*-transmitting fluids: the non-penetrating silicone oil and the potentially pore-penetrating methanol:ethanol:H_2O = 16:3:1 mixture, ethylene glycol and 2methyl-2propen-1ol. The high-pressure experiment in silicone oil shows a remarkable flexibility of the FER framework. Two displacive phase transitions, following the path *Pmnn*-to-$P12_1/n1$-to-$P2_1/n11$ with pressure, were observed. The three polymorphs were found to share a virtually identical bulk elastic behavior, though showing a different anisotropic pattern. The experiments with potentially penetrating media enhanced the occurrence of a complex scenario, from which the *P*-induced intrusion of fluid molecules into the FER structural voids can be assumed by the different phase-transition paths and compressibility patterns, by the calculated residual electron density and by the different deformation mechanisms at the atomic scale, observed as a function of the used medium. The starting orthorhombic polymorph was always restored upon decompression in all the experiments. The roles of the different surface area in single crystal and polycrystalline samples, and of the process kinetics on the compressibility and crystal-fluid interactions, are discussed.

Keywords

Ferrierite; synchrotron XRD; high pressure; *P*-induced molecule intrusion; displacive phase transition.

1- Introduction

In the last years, a significant number of studies has been devoted to the behavior of natural and synthetic zeolites under pressure (H*P*), e.g. [1,2] and references therein. These materials respond to pressure with a variety of behaviors sometimes even unexpected. For instance, comparative elastic analysis [1 and references therein] shows that microporosity does not necessarily imply high compressibility: several zeolites – due to their extraframework content and to the interactions between the host framework and guest species - are less compressible than other non-zeolitic and denser silicates. Concerning synthetic porous materials, the effects of applied pressure and molecular spatial confinement can open interesting scenarios. Pressure can play an important role in increasing the efficiency of zeolites as "nano-reactors" in the field of heterogeneous catalysis, favoring the access of reactants and products to/from the catalytically active sites and the aggregation of molecules in the microporous cavities.

To determine the exploitability and the efficiency of a porous material in H*P* processes, it is essential to study its elastic behavior and the *P*-induced structural deformations under a series of experimental conditions, e.g. different *P* regimes and different *P*-transmitting fluids (PTF). In particular, it is well known that H*P* studies on porous materials can be performed using penetrating or non-penetrating PTF [3]. The former are usually aqueous/organic mixtures, with molecular sizes small enough to penetrate the zeolite pores, e.g. [1,4,5] for a review; the latter are usually molecules too large to penetrate the zeolitic cavities, e.g. [6-9]. While non-penetrating PTF are mainly used to study the zeolites compressibility, along with *P*-induced phase transitions and

amorphization, the penetrating ones can be used for investigating the *P*-induced intrusion of extra-guest molecules in the framework pores, e.g. [7,10]. In particular, H_2O intrusion in hydrophobic all-silica zeolites is of interest, e.g. to understand the crystal-fluid interactions at the atomic scale in fundamental sciences and in potential technological applications (e.g. inhibition of corrosion, heterogeneous catalysis, water purification). According to the reversible or irreversible character of the intrusion–extrusion cycle, the 'water–Si zeolite' systems are able to restore, absorb or dissipate mechanical energy. Consequently, molecular 'spring', 'damper' or 'shock absorber behavior can be observed, e.g. [11-14].

Beyond H_2O condensation inside zeolite cavities, also the hyper-confinement of other guest molecules has been recently studied. It has been shown that the application of external pressure produces the shortening of the intermolecular distances of confined organic molecules (e.g. ethylene, acetylene) hosted in zeolite channels, inducing polymerization reactions without catalysts or radical initiators [15,16].

The *P*-induced intrusion phenomena - beyond favoring the supramolecular organization of the guest species inside the zeolite - have been shown to have also important implications on the overall elastic behavior of the material, as the new guest molecules generally contribute to stiffen the structure, hindering the *P*-induced deformations [17-19].

In this paper, we explore – by synchrotron X-ray single-crystal (SC-XRD) and powder diffraction (XRPD) and using a number of penetrating and non-penetrating PTF – the compressibility and the crystal-fluid interactions upon pressure of a siliceous

compound with ferrierite topology, characterized by a neutral SiO_2 framework and expected to favor the penetration of liophilic/hydrophobic guest species [20].

Ferrierite (framework type FER, topological symmetry: *Immm*, idealized unit-cell parameters: a = 19.0 Å, b = 14.3 Å, c = 7.5 Å, [21]) is both a well-known zeolite mineral [22,23] and a synthetic porous material, prepared readily by both aqueous [24] and non-aqueous routes [25]. Its crystal structure [26-28] (Figure 1) consists of rings of five SiO_4 tetrahedra (known as five-membered rings building units), which form layers on the **ab** plane. The layers are connected to form ten-membered rings (10MR), channels running parallel to [001] (Figure 1), which are intersected by 8MR channels running along [010] (Figure 1). Six-membered rings connect the 10MRs channels along [010] (Figure 1). The structure contains cavities known as *fer* cages, formed by the intersection of the eight-membered ring channels and the six-membered ring cavities parallel to the **c**-axis.

Ferrierite is used in the petrochemical industry as a shape selective catalyst for the production of isobutene [29]. In its Si-rich form, ferrierite has also been used for water purification [30,31] and for the selective adsorption of alkanes [20].

The first H*P* study of ferrierite has been recently published by Arletti et al. [32]. A natural ferrierite from Monastir (Sardinia, Italy) and its synthetic pure-silica counterpart (hereafter Si-FER) were investigated by means of in situ synchrotron X-ray powder diffraction (XRPD), using penetrating (methanol:ethanol:water 16:3:1, hereafter m.e.w.) and non-penetrating (silicone oil, hereafter s.o.) PTF. Evidence of H_2O molecules penetration during compression of Si-FER in m.e.w was found. The refinement performed at 0.2 GPa enabled the location of 15 H_2O molecules, forming

bulk-like and monodimensional H_2O clusters. On the contrary, neither methanol or ethanol penetration was observed.

The aim of this study is to explore the response to applied pressure of Si-FER by single crystal and powder synchrotron X-ray diffraction, using a series of potentially penetrating and non-penetrating PTF. The following aspects will be discussed:

1. the structural deformations at the atomic scale induced by compression;
2. the elastic behavior in response to the applied pressure;
3. the potential penetration process of H_2O and/or other organic guest molecules;
4. the reversibility of the observed phenomena;
5. the comparison between the overall elastic behavior of Si-FER and those of other siliceous zeolites;
6. the role played by the different surface area in single crystal and polycrystalline samples and by the process kinetics on the compressibility and crystal-fluid interactions

Moreover, the single-crystal structure refinements here performed on the data of Si-FER compressed in m.e.w. will allow integrating the results obtained in the previous powder study by Arletti et al. [32], with further atomic-scale descriptions of the *P*-induced deformation mechanisms.

2 - Materials and experimental methods

The Si-FER here investigated was synthesized according to the protocol reported in Rakoczy et al. [33]. Electron microprobe and thermogravimetric analyses [32]

confirmed the expected chemical formula ($Si_{36}O_{72}$) and the absence of template molecules within the structural voids.

2.1 - H*P* single-crystal X-ray diffraction experiments

The in situ H*P* single-crystal X-ray diffraction experiments were performed at the ID09A beamline of the European Synchrotron Radiation Facility (ESRF) in Grenoble, France. Transparent and euhedral crystals, approximately 30·30·20 μm^3 in size, were selected among the synthesis product. For each H*P*-experiment, a single crystal of Si-FER was loaded, along with few ruby chips as *P*-calibrants (*P*-precision between 0.02 and 0.09 GPa; [34,35]), in a membrane-driven diamond anvil cell (DAC), mounting Boehler-Almax-design diamonds (culet diameter: 600 μm). The *P*-chamber (250 μm in diameter) was drilled by spark-erosion in steel gaskets, previously pre-indented to ca. 70 μm. Four in situ H*P*-experiments were performed using different *P*-transmitting fluids: 1) silicone oil (s.o.), 2) 16:3:1 = methanol:ethanol:H_2O mixture (m.e.w.), 3) ethylene glycol ($HOCH_2CH_2OH$, hereafter e.gl.) and 4) 2methyl-2propen-1ol [$CH_2C(CH_3)CH_2OH$, hereafter m.p.o.]. Due to the large size of the molecules, silicone oil is a "non-penetrating" fluid. On the contrary, m.e.w., e.gl. and m.p.o. may potentially penetrate through the zeolite pores. The description of the experimental setup is reported in detail by Merlini and Hanfland [36]: a parallel monochromatic beam, with E = 30 keV (λ = 0.414 Å) was vertically focused by a spherical mirror and horizontally by a bent Si-(111) monochromator. The diffraction patterns were collected by a MAR555 flat-panel detector. At any pressure point, the same data collection protocol was applied: an ω-rotation of the DAC between -30° and +30°, with 1° rotation step and 1 s/frame exposure time. The collected diffraction patterns were analyzed using

the *Crysalis* software [37]. The unit-cell parameters were determined, from any dataset, by least-squares refinement based on the position of the diffracted peaks. The structure refinements, based on the peak intensities corrected for Lorentz-polarization effect and for absorption of the DAC components (using the semi-empirical *ABSPACK* routine implemented in *Crysalis*), were performed using the *JANA2006* software [38]. For the silicone oil experiment, the structure refinements of three observed polimorphs (see section 3.1) were performed starting from the atomic site positions found using the *SUPERFLIP* program [39], implemented in *JANA2006*. The crystal structures of the *Pmnn* and $P12_1/n1$ polymorphs (see section 3.1) were refined using independent isotropic displacement parameters (*idp*'s) for any atomic position. Due to a lower number of observed reflections (Table 1) and, more in general, to a lower quality of the H*P* diffraction data, for the $P2_1/n11$ polymorph the nine Si sites were restrained to share the same *idp* and the same was applied to the eighteen oxygen atoms (Table 2). At any pressure point, soft restraints to the intra-tetrahedral bond distances were applied (with Si-O = 1.61±0.02 Å). All the refinements converged with no significant correlations among the refined parameters and with residual peaks in the difference-Fourier maps of electron density ≤ |1.5| $e^-/Å^3$. Further details on the structure refinements are reported in Tables 1, 2 (site coordinates and *idp*'s) and 3 (relevant structural parameters).

2.2 - H*P* X-ray Powder Diffraction experiments

XRPD experiments were performed at the SNBL1 (BM01a) beamline at ESRF using modified Merril-Bassett DACs [40]. Two different experiments were performed, using ethylene glycol and 2methyl-2propen-1ol. Pressure was calibrated using the ruby

fluorescence method [41], on the non-linear hydrostatic pressure scale [34]. The estimated *P*-precision was 0.05 GPa. The diffraction data were collected in the Debye–Scherrer geometry on a Dectris 2M Pilatus image plate. One-dimensional diffraction patterns were obtained by integrating the two dimensional images with the *FIT2D* software [42]. Rietveld full-profile fitting was performed using the *GSAS* package [43] with the *EXPGUI* [44] interface. The starting atomic coordinates for the orthorhombic structure were taken from the structural model of Morris et al. [28]. The background curve was fitted by a Chebyshew polynomial with 20 coefficients. The pseudo-Voigt profile function by Thomson et al. [45] was applied, and the peak intensity cut-off was set to 0.1% of the peak maximum. The unit-cell parameters were allowed to vary for all refinement cycles.

The experiments were performed from 0.2 GPa to 3.4 GPa and to 6.2 GPa for compression in e.gl. and m.p.o., respectively. Some patterns were also collected upon decompression from the highest pressure to P_{amb} for all the experiments. Unit-cell parameters were determined by Rietveld profile fitting up to 3.4 and 5.2 GPa for e.gl. and m.p.o. experiments, respectively, as for the m.p.o. experiment, the data quality at higher pressures did not allow reliable refinements. Details of the structure refinements are reported in Tables 1d and 2d (deposited); while selected integrated patterns from the two ramps are reported in Figure 2.

3 – Results

3.1 – Single crystal H*P*-experiment in silicone oil

The *P*-induced evolution of the unit-cell parameters of Si-FER compressed in s.o. is reported in Table 4 and is shown in Figure 3. These experimental data show a remarkable flexibility of the ferrierite framework at high pressure. A first displacive phase transition occurs from the orthorhombic space group *Pmnn* to the monoclinic subgroup $P12_1/n1$ at ~ 0.7 GPa, as confirmed by the reflection conditions shown in Figure 4. A pseudo-orthorhombic twinning, favored by $\beta \approx 90°$ (Table 4), is found with refined twins ratio 0.77(1):0.23(1). A second displacive phase transition, involving a significant unit-cell volume contraction (Figure 3), is observed at ~ 1.24 GPa from the $P12_1/n1$ to the $P2_1/n11$ space group: *i.e.* with a switch of the monoclinic axis from **b** to **a**. Since the former monoclinic space groups do not share a group-subgroup relationship (*International Tables for Crystallography Vol. A* [46]), such a multistage displacive phase transition is necessarily achieved through an intermediate structure with a *P*-1 symmetry, being the latter the only common subgroup of both $P12_1/n1$ and $P2_1/n11$ ("type-II" transition according to Christy [47,48]). The reconstruction of the 0*kl** reciprocal plane, reported in Figure 4, shows a clear split of the diffraction spots following the second phase transition, due to the occurrence of four twin domains. The high-*P* $P2_1/n11$ polymorph is stable at least up to 3.00(7) GPa (Figure 3, Table 4), where a decrease in intensity and a broadening of the diffraction peaks suggested an impending deterioration of the long-range order of the investigated crystal, even in response to the non-hydrostaticity of s.o. at this pressure [49].

The three Si-FER polymorphs share a virtually identical bulk elastic behavior, being their average volume compressibilities $\beta_V = (1/V_{P\max}\text{-}V_{P\min})\cdot(V_{P\max}\text{-}V_{P\min}/P_{\max}\text{-}P_{\min})$: 0.051(4), 0.056(9) and 0.055(3) GPa^{-1}, for the *Pmnn*, $P12_1/n1$ and $P2_1/n11$

polymorphs, respectively (P_{min}-P_{max} are P_1-P_3, P_4-P_6 and P_7-P_{12}, respectively, Table 4). The components of the unit-strain tensor and of the related compressibility tensor, for any polymorph, were calculated between the lowest and the highest experimental *P*-points (within the respective phase stability fields, Table 4) using the *Win_Strain* software [50]. The finite Eulerian strain tensor was adopted coupled with the following Cartesian axial system: **x**//**a*** and **z**//**c**. The magnitude and the orientation of the principal coefficients of the compressibility tensor for the three polymorphs (with $|\varepsilon_3| > |\varepsilon_2| > |\varepsilon_1|$) are reported: 1) *Pmnn*: ε_3//**a** = 0.025(2) GPa^{-1}, ε_2//**c** = 0.016(1) GPa^{-1}, ε_1//**b** = 0.0111(8) GPa^{-1}; 2) $P12_1/n1$: $\varepsilon_3[\angle\mathbf{a} = 11(1)°]$ = 0.032(6) GPa^{-1}, $\varepsilon_2[\angle\mathbf{c} = 11(1)°]$ = 0.013(2) GPa^{-1}, ε_1//**b** = 0.011(2) GPa^{-1}; $P2_1/n11$: ε_3//**a** = 0.037(2) GPa^{-1}; $\varepsilon_2[\angle\mathbf{c}$ = 42.4(3)°] = 0.0162(8) GPa^{-1}, $\varepsilon_1[\angle\mathbf{b}$ = 40.0(3)°] = 0.0048(3) GPa^{-1}. The elastic anisotropy of the three polymorphs of Si-FER can, therefore, be described as ε_3: ε_2: ε_1 = 2.25:1.44:1 (for *Pmnn*), 2.91:1.18:1 (for $P12_1/n1$) and 7.71:3.38:1 (for $P2_1/n11$), with the most compressible unit-strain component always being parallel (or quasi-parallel) to the **a** crystallographic axis. The analysis of the compressibility tensors points out that the *Pmnn*-to-$P12_1/n1$ phase transition has only a minor effect on the magnitude and the orientation of the strain ellipsoid and, therefore, on the elastic behavior of Si-FER. On the contrary, the $P12_1/n1$-to-$P2_1/n11$ (via *P*-1) phase transition drastically changes the shape and the orientation of the strain ellipsoid, especially within the (100) plane, leading to a significantly more anisotropic elastic behavior.

The structure refinements of the three polymorphs show that the *P*-induced deformation at the atomic scale is mainly accommodated by the tilting of the SiO_4 tetrahedra around the shared O hinges, as expected in this class of materials [1,51]. In

the *Pmnn*-polymorph, the presence of the mirror plane at $x = 0$, centering either the 6MR[001], the 10MR[001] and the 8MR[010] (Figure 1), constrains the deformation of the two sets of channels (*i.e.* the ring diagonals are equal in length, Figure 1 and Table 3). As a consequence, in the stability field of the orthorhombic polymorph, the bulk volume contraction is accommodated by compression of the channels and of the ferrierite cages, along the three crystallographic axes. Upon the *Pmnn*-to-$P12_1/n1$ phase transition, the mirror element and, as a consequence, the symmetry constraints are lost. This allows, beside the channel and cage compression, also an "elliptical" deformation of the 6- 10- and 8-rings (Figure 1). This is described by their "deformation ratio", here defined as E = S/L (Table 3), where S and L are the shortest and longest ring diagonals, respectively (Figure 1). This deformation partially accommodates the bulk compression, as can be deduced by Figure 1, through the deviation of the O1-O1-O1 intertetrahedral angle from 180° (Table 3). The $P12_1/n1$-to-$P2_1/n11$ phase transition is coupled with a significant volume contraction (Figure 3, Table 4), which is mainly accommodated by a dramatic compression and deformation of the 8MR[010]-channels (Figure 1), as also shown by the collapse of the E-8MR[010] (Table 3), and, to a lesser extent, of the 10MR[001]-channels. In the stability field of the $P2_1/n11$ polymorph, the main deformation mechanisms at the atomic scale are basically analogous to those observed for the $P12_1/n1$ polymorph.

Upon pressure release, the orthorhombic unit cell is completely restored, as well as the *Pmnn* crystal structure (Tables 1, 2 and 3), suggesting a complete reversibility of the complex high-pressure behavior previously described.

3.2 –H*P*-experiments with potentially penetrating *P*-transmitting fluids

3.2.1 - Single-crystal experiments: unit-cell parameters *vs. P*

The H*P* behavior of Si-FER with m.e.w. as PTF was investigated up to 3.86(7) GPa, collecting data at eight experimental *P*-points (Figure 5; Table 3d-deposited). The orthorhombic *Pmnn* structure is found to be stable at least up to 0.95(2) GPa. A phase transition to the $P12_1/n1$ polymorph occurs between 0.95(2) and 1.55(2) GPa, and the monoclinic polymorph is observed up to the highest investigated pressure. The phase transition is reversible and the orthorhombic space group is restored after the pressure release.

The H*P* behavior of Si-FER, compressed in e.gl., was investigated up to 4.05(2) GPa, collecting data at twelve pressures (Figure 5, Table 3d-deposited). The orthorhombic polymorph is stable up to 0.57(1) GPa. The monoclinic $P12_1/n1$ polymorph is observed in the pressure range 0.93(2)-2.37(1) GPa, and its structure is successfully refined. Between 2.63(4) and 4.05(2) GPa, both the unit-cell parameters and the structure refinements in the monoclinic space group lead to unsatisfactory figures of merit. Since no hints for the phase transition to the $P2_1/n11$ polymorph could be found, we are inclined to consider a potential $P12_1/n1$-to-*P*-1 phase transition as likely. An attempt to refine the crystal structure of the triclinic polymorph was tried, but unsuccessfully, probably for the high number of structural variables involved. Upon decompression, the *Pmnn* polymorph is restored.

Si-FER compressed in m.p.o. (nine experimental *P*-points up to 2.08(4) GPa, Figure 5, Table 3d-deposited) shows a behavior in the low-*P* regime similar to that observed

using silicone oil and e.gl.: the *Pmnn* polymorph is stable at least up to 0.58(2) GPa. The $P12_1/n1$ polymorph is observed in the range 0.77(3)-2.08(4) GPa, with an apparent discontinuity in the elastic behavior between 1.04(5) and 1.30(1) GPa (Figure 5). Datasets collected at $P > 2.08$ GPa show a significant decrease in the quality of the diffraction peaks, which do not allow neither the refinement of the unit-cell parameters, suggesting an impending amorphization or a severe deterioration of the crystal long-range order. Upon decompression, the orthorhombic structure is fully restored.

Two further H*P* experiments were conducted on Si-FER single-crystals, using e.gl. and m.p.o. as PTF, but adopting a "fast-compression strategy": the pressure was single-step raised from room-*P* to 1.55(4) and 2.23(3) GPa, respectively. In both cases, the *Pmnn*-to-$P2_1/n11$ phase transition is observed. It is worth to remark that, in the previously described "slow" compression experiments, this H*P*-polymorph is observed at about 1.24 GPa only using s.o. as PTF.

3.2.2 - Single-crystal experiments: structure refinements at high pressure

All the refinements converged to satisfactory final agreement factors, with no significant correlation among the refined parameters. Difference-Fourier maps of the electron density were calculated for all the structure refinements, in order to locate potentially intruded molecules within the structural voids of Si-FER. In the case of the *Pmnn* and $P12_1/n1$ polymorphs observed in the experiment with m.e.w., a disordered distribution of electron density is observed at the center of the *fer* cage and, at the corresponding height (i.e. $z = 0$), within the 10MR-channels (Figure 6). The Fourier

syntheses obtained from the structure refinements of the *Pmnn* polymorphs compressed in e.gl. and m.p.o. do not allow the location of any detectable residual peak. In contrast, the syntheses from the refinements of the $P12_1/n1$ polymorphs in the same *P*-fluids show a disordered distribution of the electron density within the *fer*-cage and the 10-ring channel at $z \sim 0$, similar to that found in m.e.w. (Figure 6), coupled with weaker broad peaks in the 10MR-channel at $0.2 < z < 0.4$. The distribution of this residual electron density suggests the presence of intruded molecules within the structural voids of Si-FER, in a configuration which allows both molecule-molecule and molecule-framework interactions *via* hydrogen bonding. However, the weak intensity of these peaks ($\rho < 1.5\ e^-/Å^3$), coupled with their disordered distribution (Figure 6), do not allow a clear and unambiguous location of any atomic site, neither an unambiguous assignment of the chemical nature of the molecules. Although a direct modeling of the intruded molecules is not possible, several indirect information about the *P*-induced penetration of fluid molecules are provided by both elastic and structural data (see section 4).

3.2.3 – Powder experiments: unit-cell parameters *vs. P*

The results of the H*P* XRPD study of Si-FER using e.gl. as PTF (ten experimental *P*-points up to 3.40 GPa) are in good agreement with the single-crystal data. Between 0.6 and 0.9 GPa, the sample undergoes a phase transition to the monoclinic polymorph $P12_1/n1$, which is stable at least up to 3.40 GPa (Figure 5). Up to 0.60 GPa, the cell parameters undergo isotropic compression accounting for a volume variation of ~2% (Table 1d-deposited). At pressures above the phase transition, **a** parameter undergoes a stronger compression, accounting for a total variation of – 4.5 % at 3.4 GPa (against -

2.9 and -2.5 % of **b** and **c**, respectively, Table 1d-deposited). The phase transition is completely reversible and the orthorhombic structure is restored upon pressure release.

The H*P* study of Si-FER using m.p.o. (fifteen experimental *P*-points up to 6.27 GPa) provided a more complex scenario, especially if compared to the single-crystal data. The orthorhombic polymorph is stable up to 1.18 GPa. At higher pressures, the rising of new Bragg peaks indicates the occurrence of a phase transition. At 1.64 GPa, the two monoclinic polymorphs $P12_1/n1$ (as minor component) and $P2_1/n11$ (as major component) coexist and remain stable up to 5.25 GPa. The $P2_1/n11$ results to be the most compressible polymorph, showing a total volume variation of – 18.7% at 5.25 GPa (against -13.3% of the $P12_1/n1$ polymorph). Datasets collected at $P > 5.25$ GPa showed a significant decrease in the quality of the diffraction data, which does not allow neither the refinement of the unit-cell parameters, suggesting a deterioration of the structural long-range order. Upon pressure release, the orthorhombic structure is fully restored.

4 - Discussion

The analysis of the complex H*P* behavior of Si-FER shows different compressibility values and diverse phase-transition paths depending on the process kinetics and on the nature of the *P*-transmitting fluids.

Compression using silicone oil as non-penetrating PTF evidences a remarkable flexibility of the [FER]-framework, which undergoes two changes in symmetry through displacive phase transitions, with preservation of crystallinity at least up to 3.00(7) GPa (Figure 3; Table 4). Similar results were found also by Arletti et al. [32] for the same

sample, even though in that experiment only one phase transition (to *P*121/*n*1) was clearly observed. These data may be coupled with the results obtained from a high-temperature X-ray diffraction study of Si-FER [52], which show the occurrence of a displacive phase transition from the starting *Pmnn* space group to *Immm* at 400 K. In this light, the following phase-transitions path may be proposed for siliceous ferrierite at varying *T* and *P*:

$$Immm \leftarrow (\uparrow \text{Temp.})\ Pmnn\ (\uparrow \text{Pres.}) \rightarrow P12_1/n1 \rightarrow (P\text{-}1) \rightarrow P2_1/n11$$

where *Pmnn* is the stable polymorph at ambient conditions and *P*-1 is a necessary transient state between the $P12_1/n1$-to-$P2_1/n11$ phase transition (type-II phase transitions of Christy [47,48]).

A common feature of the experiments performed with the different PTF is the occurrence of the *Pmnn*-to-$P12_1/n1$ phase transition at about 0.7 GPa, except for the m.e.w. experiment (Figure 5), where it occurs at a significantly higher pressure (~ 1.5 and 1.8 GPa for single crystal and powder experiment, respectively), and for the powder experiment with m.p.o. (see below). Beside this, the *Pmnn*-polymorphs show comparable *P*-*V* patterns in silicone oil, e.gl. and m.p.o. (with a slight deviation only approaching the transition-*P*, Figure 7), suggesting the absence - or the irrelevance - of molecule intrusion from ethylene glycol and 2methyl-2propen-1ol fluids. On the contrary, the *P*-*V* pattern observed in SC and powder experiments with m.e.w. (Figures 5 and 7), is characterized by higher unit-cell volumes (at comparable pressures), which suggest a *P*-induced penetration of molecules at a very low-*P* regime. This is also confirmed by the intensity ratio of the first diffraction peaks (i.e. at low θ-value) of the XRPD patterns, the most sensitive to the extraframework content and distribution. In

fact, while in the experiments performed in e.gl. and m.p.o. their ratios remain almost constant up to the phase transition pressure (above which some changes are observed, Figure 2), in m.e.w. their intensity ratio varies significantly also in the low-*P* regime [32]. This is in agreement with Cailliez et al. [11], who reported the occurrence of H_2O intrusion at 100 MPa, based on mercury porosimetry analysis and molecular simulations. The significantly higher *Pmnn*-to-$P12_1/n1$ phase transition pressure in m.e.w., if compared to the experiments with the other three aforementioned *P*-fluids (Figure 5), further suggests the occurrence of a crystal-fluid interaction which leads to a significant "extension" of the *P*-stability field of the orthorhombic polymorph. Arletti et al. [32], by in situ synchrotron XRPD H*P*-experiment on the same sample, found the *P*-induced penetration of about fifteen H_2O molecules per unit cell at 0.2 GPa. The position of the five independent H_2O-sites is in fair agreement with the spatial distribution of the residual electron density maxima of the *Pmnn*-polymorph based on the single-crystal refinements of this study. In addition, the slightly different *P*-*V* trends observed for single crystal and powder (in m.e.w., Figure 5) reflect a different crystal-fluid interaction. In fact, the higher compressibility observed from the single crystal data suggests a modest molecule penetration if compared to the polycrystalline sample. This is likely due to the higher surface area of the powder, which may significantly enhance the *P*-induced intrusion of fluid molecules.

Excluding the XRPD data in m.p.o., the H*P* $P2_1/n11$ polymorph has never been observed compressing Si-FER in pore-penetrating fluids and, as a consequence, the stability field of the intermediate $P12_1/n1$-polymorph was found to be significantly different in pressure (Figures 5 and 7, Tables 1d, 2d and 3d [deposited]). Moreover, the

analysis of all the experimental *P*-*V* data clearly shows the occurrence of different compressibility patterns in response to the nature of the PTF and, in part, to the use of single crystal or polycrystalline samples, as discussed in the previous paragraph. The following considerations can be done:

1) the compressibility of Si-FER in s.o. is significantly higher than that in the other PTF, mainly due to the occurrence of the $P12_1/n1$-to-$P2_1/n11$ phase transition and to the absence of fluid penetration;

2) from SC- and powder-data, the compressibility of the $P12_1/n1$-polymorph in e.gl. is lower than that of the same polymorph in the other penetrating *P*-fluids (Figures 5 and 7), suggesting the onset of a *P*-induced molecule penetration above the *Pmnn*-to-$P12_1/n1$ transition pressure, according to the broad peaks found in the difference electron density map (Figure 6).

3) The direct *Pmnn*-to-$P2_1/n11$ phase transition observed during the single-step compression (from room-*P* to 1.5-2.0 GPa) of Si-FER single crystals in e.gl. and m.p.o. suggests that kinetics is also a fundamental variable influencing the crystal-fluid interactions at high pressure.

The H*P* behavior of Si-FER in m.p.o. deserves further considerations, especially for the different results obtained from the SC- and powder-diffraction experiments. The SC-data show a behavior comparable to that observed in s.o., except for an apparent discontinuity in the *P*-*V* data between 1.04(5) and 1.30(1) GPa, which may be explained by a modest molecules intrusion, as corroborated by the weak peaks in the difference-Fourier maps of electron density (Figure 6). The powder data show that the *Pmnn*-polymorph results to be stable up to 1.18(5) GPa. Above this pressure, the co-existence

of the $P2_1/n11$ (as a major component) and $P12_1/n1$ (as a minor component) polymorphs is observed. In addition, the compressibility of the $P12_1/n1$-polymorph is lower than that obtained from the SC-data (Figure 5). These data suggest that a fraction of the Si-FER polycrystalline sample does not experience the *P*-induced intrusion of m.p.o. molecules, leading to the *Pmnn*-to-$P2_1/n11$ (via $P12_1/n1$ and *P*-1) phase transition. On the other hand, the *P*-induced intrusion of m.p.o. molecules likely involves a minor fraction of the crystallites, which do experience the *Pmnn*-to-$P12_1/n1$ phase transition showing a lower compressibility.

Based on these results, we suggest that: *i)* a fast kinetics may prevent the *P*-induced molecule intrusion, leading to the highly compressed $P2_1/n11$ polymorph and, on the other hand, *ii)* in the experiments where the extension of the $P12_1/n1$ stability field is observed, the *P*-induced penetration of the fluid molecules may be reasonably assumed.

As reported in the previous section, the SC-data did not allow an unambiguous structural characterization of the intruded molecules. However, some information can be extracted from the atomic scale analysis of the framework deformation mechanisms. In particular, we will focus on the "elliptical" deformation of the 6-, 8- and 10-rings of tetrahedra (Figure 1). This mechanism takes place only after the disappearance of the mirror plane at $x = 0$, i.e. following the *Pmnn*-to-$P12_1/n1$ phase transition. Table 3 reports the evolution with pressure of the "deformation parameters" E = S/L (S and L: shortest and longest diameters, respectively) of the 6-, 8- and 10-rings of Si-FER from the H*P*-experiments. These data show that the 6- and 10-rings of Si-FER compressed in e.gl. and m.p.o. experience a higher "elliptical" deformation if compared to that observed in s.o. and m.e.w. at comparable pressures (Figure 8). Similarly, the 8-rings,

which define the access to the *fer*-cage from the 10MR-channels, show a slight, but significant, deformation in the samples compressed in s.o. and m.e.w., but are almost undistorted when compressed in e.gl. and m.p.o. (Figure 8, Table 3). These experimental findings suggest the occurrence of different crystal-fluid interactions able to influence the framework deformation mechanisms, likely ascribable to the *P*-induced penetration of molecules from the fluid into the structural pores of the zeolite. The disordered distribution of the residual electron density (Figure 6) suggests the occurrence of several partially occupied extraframework sites, where clusters of molecules can be hosted, in agreement with the previous findings of Arletti et al. [32], based on in situ synchrotron powder diffraction data, and Caillez et al. [11], based on molecular simulations.

5 – Concluding remarks

This H*P* study demonstrates the remarkable flexibility of Si-FER, an industrially important porous material. Coupling our results with those from Bull et al. [52], the following symmetry changes can be proposed for pure siliceous ferrierite at varying *T* and *P*:

$$Immm \leftarrow (\uparrow\text{Temp.})\ Pmnn\ (\uparrow\text{Pres.}) \rightarrow P12_1/n1 \rightarrow (P\text{-}1) \rightarrow P2_1/n11,$$

where *Pmnn* is the stable polymorph at ambient conditions.

It is worth to note that in Al-bearing ferrierites, the structure symmetry is also governed by the nature and the location of the extraframework components, as confirmed by the different space groups reported in the literature for natural or synthetic samples: *Immm* [e.g. 53-55], *I*222 [56], *Pnnm* [27] and $P12_1/n1$ [57].

The high-pressure study of Si-FER using different potentially penetrating PTF showed the occurrence of a complex behavior in response to the nature of the *P*-transmitting fluid, to the single-crystal or polycrystalline nature of the sample (likely for the different surface areas) and to the process kinetics. The results obtained in this study confirm the *P*-induced penetration of H_2O molecules (and potentially methanol and ethanol) at a very low-*P* regime ($P < 0.2$ GPa), in fair agreement with the findings of Caillez et al. [11] and Arletti et al. [32]. On the contrary, the *P*-induced penetration of e.gl. and m.p.o. molecules in the Si-FER structural voids is likely prevented at pressures below the *Pmnn*-to-$P12_1/n1$ phase transition - observed at about 0.6 GPa - but occurs in the high-pressure polymorphs. The reversible nature of the *Pmnn*-to-$P12_1/n1$ phase transition and the potential reversibility of the related *P*-induced molecules intrusion may arise the interest on these systems in the field of the energy storage: the mechanical energy required to promote the molecule intrusion (generally H_2O) can be completely or partially restored to the system by the extrusion of the same molecules upon decompression, when the phenomenon is completely or partially reversible, respectively, e.g. [58-60].

If we compare the H*P* behavior of the high-silica zeolites compressed in s.o. reported in literature, it results that Si-FER is one of the less compressible. In fact, in the range P_{amb}-1.2 GPa (selected for an easy comparison) the volume variation is -4.09% in Si-FER [32], -6.4% in HS-MOR [61], -5% in silicalite-1 F and -6.6% in silicalite-1 OH [10]. Only all-silica Y [62] shows a lower volume variation: i.e. -2.6%. These results confirm, once again, that zeolite compressibility is not simply related to the material porosity, expressed by the "framework density" (FD, [21]). Specifically, Si-FER (FD =

17.6 T/1000 Å^3) is unexpectedly more compressible than siliceous zeolite-Y, which is characterized by the lowest FD (13.3 T/1000 Å^3) among the aforementioned compounds.

6 - Acknowledgements

ESRF is acknowledged for the allocation of beamtime. This research was funded by the Italian Ministry of Education, MIUR Projects: "Futuro in Ricerca 2012 – ImPACT-RBFR12CLQD" and "PRIN 2010-11 – Dalle materie prime del sistema Terra alle applicazioni tecnologiche: studi cristallochimici e strutturali".

7 - References

[1] G.D. Gatta, Y. Lee, Mineral. Mag. 78 (2014) 267-291.

[2] G. Vezzalini, R. Arletti, S. Quartieri, Acta Cryst. B70 (2014) 444–451.

[3] G.D. Gatta, Z. Kristallogr. 223 (2008) 160-170.

[4] C. Betti, E. Fois, E. Mazzucato, C. Medici, S. Quartieri, G. Tabacchi, G. Vezzalini, V. Dmitriev, Micropor. Mesopor. Mater. 103 (2007) 190–209.

[5] S. Ori, S. Quartieri, G. Vezzalini, V. Dmitriev, Am. Mineral. 93 (2008) 1393-1403.

[6] R. Arletti, S. Quartieri, G. Vezzalini, Am. Mineral. 95 (2010) 1247-1256.

[7] R. Arletti, G. Vezzalini, A. Morsli, F. Di Renzo, V. Dmitriev, S. Quartieri, Micropor. Mesopor. Mater. 142 (2011) 697–707.

[8] E. Fois, A. Gamba, C. Medici, G. Tabacchi, S. Quartieri, E. Mazzucato, R. Arletti, G. Vezzalini, V. Dmitriev, Micropor. Mesopor. Mater. 115 (2008) 267-280.

[9] L. Leardini, S. Quartieri, G. Vezzalini, Micropor. Mesopor. Mater. 127 (2010) 219–227.

[10] S. Quartieri, G. Montagna, R. Arletti, G. Vezzalini, J. Solid State Chem. 184 (2011) 1505–1516.

[11] F. Cailliez, M. Trzpit, M. Soulard, I. Demachy, A. Boutin, J. Patarin, A.H. Fuchs, Phys. Chem. Chem. Phys 10 (2008) 4817–4826

[12] P. Demontis, G. Stara, G.B. Suffritti, J. Phys. Chem. B 107 (2003) 4426-4436

[13] N. Desbiens, I. Demachy, A.H. Fuchs, H.K. Rodeschini, M. Soulard, J. Patarin, Angew. Chem. Int. Ed. 44 (2005) 5310 –5313

[14] M. Trzpit, M. Soulard, J. Patarin, N. Desbiens, F. Cailliez, A. Boutin, I. Demachy, A.H. Fuchs Langmuir 23 (2007) 10131-10139

[15] M. Santoro, F.A. Gorelli, R. Bini, J. Haines, A. Van der Lee, Nat. Commun. 4 (2013) 1557-1563.

[16] D. Scelta, M. Ceppatelli, M. Santoro, R. Bini, F.A. Gorelli, A. Perucchi, M. Mezouar, A. Van der Lee, J. Haines, Chem. Mater. 26 (2014) 2249−2255.

[17] E. Fois, A. Gamba, G. Tabacchi, R. Arletti, S. Quartieri, G. Vezzalini, Am. Mineral. 90 (2005) 28–35.

[18] E. Fois, A. Gamba, G. Tabacchi, S. Quartieri, R. Arletti, G. Vezzalini, in: A. Gamba, C. Colella, S. Coluccia (Eds.), Stud. Surf. Sci. Catal., vol. 155, Elsevier, Amsterdam, 2005, pp. 271–280.

[19] G.D. Gatta, Eur. J. Mineral. 17 (2005) 411-422.

[20] B. Qian, H. Jiang, Y. Sun, Y. Long, Langmuir 17 (2001) 1119-1125

[21] C. Baerlocher, L.B. McCusker, D.H. Olson, Atlas of Zeolite Framework Types,

sixth ed., Elsevier, Amsterdam, 2007.

[22] G. Gottardi, E. Galli, Natural Zeolites, Springer-Verlag, Berlin, 1985.

[23] W.S. Wise, R.W Tschernich, Am. Mineral. 61 (1976) 60 – 66.

[24] H. Gies, R.P. Gunawardane, Zeolites 7 (1987) 442 – 445.

[25] A. Kuperman, S. Nadimi, S. Oliver, G.A. Ozin, J.M. Garces, M.M. Olken, Nature 365 (1993) 239 - 242.

[26] P.A. Vaughan, Acta Cryst. 21 (1966) 983-990.

[27] A. Alberti, C. Sabelli, Z. Kristallogr. 178 (1987) 249- 256.

[28] R.E. Morris, S.J. Weigel, N.J. Henson, L.M. Bull, M.T. Janicke, B.F. Chmelka, A.K. Cheetham, J. Am. Chem. Soc. 116 (1994) 11849-11855.

[29] K. Yamahara, K. Okazaki, K. Kawanura, Catal. Today 23 (1995) 397- 402

[30] R.M. Eissmann, M.D. Le Van, Ind. Eng. Chem. Res. 32 (1993) 2752-2757.

[31] J. Stelzer, M. Paulus, M. Hunger, J. Weitkamp, Micropor. Mesopor. Mater. 22 (1998) 1-8.

[32] R. Arletti, G. Vezzalini, S. Quartieri, F. Di Renzo, V. Dmitriev, Micropor. Mesopor. Mater. 191 (2014) 27-37.

[33] R.A. Rakoczy, Y. Traa, P. Kortunov, S. Vasenkov, J. Kärger, J. Weitkamp, Micropor. Mesopor. Mater. 104 (2007) 179–184.

[34] H.K. Mao, J. Xu, P.M. Bell, J. Geophys. Res.91 (1986) 4673-4676.

[35] J.C. Chervin, B. Canny, M. Mancinelli, High Pressure Res.21 (2001) 302-314

[36] M. Merlini, M. Hanfland, High Pressure Res.33 (2013) 511-522

[37] Agilent, Xcalibur CCD System, Crysalis Software System, 2012

[38] V. Petricek, M. Dusak, L. Palatinus, Z. Kristallogr. 229 (2014) 345-352

[39] L. Palatinus, G. Chapuis, J. Appl. Crystallogr.41 (2007) 786-790

[40] R. Miletich, D.R. Allan, W.F. Kush, in: R.M. Hazen, R.T. Downs (Eds.), High Temperature and High Pressure Crystal Chemistry, Reviews in Mineralogy and Geochemistry, vol. 41, Mineralogical Society of America and Geochemical Society, Washington D.C., USA, 2000, pp. 445–519

[41] R.A. Forman, G.J. Piermarini, J.D. Barnett, S. Block, Science 176 (1972) 4673–4676

[42] A.P. Hammersley, S.O. Svensson, A. Thomson, Nucl. Instrum. Methods Phys. Res. A 346 (1994) 312–321

[43] A.C. Larson, R.B. von Dreele, Report LAUR 86, 1994

[44] B.H. Toby, J. Appl. Crystallogr. 34 (2001) 210–213

[45] P. Thomson, D.E. Cox, J.B. Hastings, J. Appl. Crystallogr. 20 (1987) 79–83

[46] T. Hahn, International Tables for Crystallography. Volume A: Space-group symmetry, fifth ed.,Springer, Dordrecht, 2002

[47] A.G. Christy, Acta Cryst. B49 (1993) 987-996

[48] A.G. Christy, Acta Cryst. B51 (1995) 753-757

[49] R.J. Angel, M. Bujak, J. Zhao, G.D. Gatta, S.J. Jacobsen, J. Appl. Crystallogr. 40 (2007) 26-32

[50] R.J. Angel, Win_Strain Users Manual. A program to calculate strain tensors from unit-cell parameters. http://www.rossangel.com 2011

[51] G.D. Gatta, Micropor. Mesopor. Mater.128 (2010) 78-84

[52] I. Bull, P. Lightfoot, L.A. Villaescusa, L.M. Bull, R.K.B. Gover, J.S.O. Evans, R.E. Morris, J. Am. Chem. Soc.125 (2003) 4342-4349

[53] R. Gramlich-Meier, W.M. Meier, B.K. Smith, Z. Kristallogr.169 (1984) 201-210

[54] M.C. Dalconi, G. Cruciani, A. Alberti, P. Ciambelli, M.T. Rapacciuolo, Micropor. Mesopor. Mater. 39 (2000) 423-430

[55] M.C. Dalconi, A. Alberti, G. Cruciani, P. Ciambelli, E. Fonda, Micropor. Mesopor. Mater. 62 (2003) 191-200

[56] Y. Yokomori, J. Wachsmuth, K. Nishi, Micropor. Mesopor. Mater. 50 (2001) 137-143

[57] R. Gramlich-Meier, V. Gramlich, W.M. Meier, Am. Mineral. 70 (1985) 619-623

[58] V. Eroshenko, R.C. Regis, M. Soulard, J. Patarin, J. Am. Chem. Soc. 123 (2001) 8129-8130

[59] A. Ryzhikov, I. Khay, H. Nouali, T.J. Daou, J. Patarin, Phys. Chem. Chem. Phys. 16 (2014) 17893-17899

[60] I. Khay, T.J. Daou, H. Nouali, A. Ryzhikov, S. Rigolet, J. Patarin, J. Phys. Chem. C 118 (2014) 3935-3941

[61] L. Leardini, S. Quartieri, R. Arletti, G. Vezzalini, High-Si mordenite: compressibility, *P*-induced amorphization and guest molecules penetration, FEZA Congress (2014) Leipzig 8-11 September, pag. 482.

[62] M. Colligan, P.M. Forster, A.K. Cheetham, Y. Lee, T. Vogt, J.A. Hriljac, J. Am. Chem. Soc. 126 (2004) 12015-12022

Table 1. Details pertaining to selected single-crystal data collections and structure refinements of Si-FER, using silicone oil as *P*-transmitting fluid.

***P* (GPa)**	**0.38(2)**	**0.64(2)**	**0.77(3)**	**1.13(5)**	**1.35(8)**	**3.00(7)**	**0.0001***
	P_1	**P_3**	**P_4**	**P_6**	**P_7**	**P_{12}**	**P_{REV}**
Space group	*Pmnn*	*Pmnn*	$P12_1/n1$	$P12_1/n1$	$P2_1/n11$	$P2_1/n11$	*Pmnn*
min≤ *h* ≤ max	-5; 7	-5; 6	-5; 6	-5; 6	-5; 6	-5; 6	-5; 7
min≤ *k* ≤ max	-18; 18	-18; 18	-18; 18	-17; 18	-17; 18	-17; 17	-20; 20
min≤ *l* ≤ max	-8; 9	-8; 9	-8; 9	-8; 9	-8; 8	-8; 8	-10; 10
Unique reflections	819	797	1419	1344	1213	1087	912
Observed reflections	563	543	905	808	480	321	450
R_{int}(obs)	0.0435	0.0440	0.0520	0.0917	0.0708	0.0457	0.0575
R_{int}(all)	0.0459	0.0467	0.0555	0.0989	0.0885	0.0739	0.0643
Number of l.s. parameters	56	56	110	110	85	85	56
R_1(obs)	0.0520	0.0564	0.0703	0.1094	0.0938	0.0926	0.0627
R_1(all)	0.0739	0.0797	0.1045	0.1573	0.1730	0.2232	0.1209
wR_1(obs);	0.0573	0.0616	0.0715	0.1143	0.1006	0.0956	0.0629
***w*R_1(all)**	0.0584	0.0626	0.0730	0.1166	0.1034	0.1010	0.0653
Residuals	+0.53	+0.51	+0.52	+1.42	+1.14	+1.34	+0.65
(e^-/Å^3)	-0.35	-0.39	-0.45	-0.95	-1.17	-1.07	-0.52

* Upon decompression; $R_{int} = \Sigma|F^2_{obs} - F^2_{obs}(mean)|/\Sigma(F^2_{obs})$;

$R_1 = \Sigma(|F_{obs} - F_{calc}|)/\Sigma|F_{obs}|$; $wR^2 = (\Sigma(w(F^2_{obs} - F^2_{calc})^2)/\Sigma(w(F^2_{obs})^2)^{0.5}$, $w = 1/(\sigma^2(F^2_{obs}))$.

Table 2. Atomic fractional coordinates and isotropic displacement parameters (U_{iso}) ($Å^2$) of the *Pmnn*, $P12_1/n1$ and $P2_1/n11$ polymorphs of Si-FER, from selected structure refinements (P_1 = 0.38(2) GPa, P_3 = 0.64(2) GPa, P_4 = 0.77(3) GPa, P_6 = 1.13(5) GPa, P_7 = 1.35(8) GPa, P_{12} = 3.00(7) GPa, P_{REV} = 0.0001 GPa) based on single-crystal data in silicone oil.

Site	*P* (GPa)	*x*	*y*	*z*	U_{iso}
			Pmnn		
Si1	0.38(2)	0.3473(4)	0.5	0	0.0134(5)
	0.64(2)	0.3482(4)	0.5	0	0.0146(6)
	0.0001*	0.3471(5)	0.5	0	0.0123(7)
Si2	0.38(2)	0.2725(3)	0.0009(1)	-0.2082(2)	0.0122(4)
	0.64(2)	0.2729(3)	0.0012(1)	-0.2087(2)	0.0136(4)
	0.0001*	0.2727(3)	0.0006(2)	-0.2078(2)	0.0122(5)
Si3	0.38(2)	0.4182(3)	0.2996(1)	-0.0128(2)	0.0125(4)
	0.64(2)	0.4182(3)	0.2998(1)	-0.0157(2)	0.0143(5)
	0.0001*	0.4184(4)	0.2993(2)	-0.0081(4)	0.0094(5)
Si4	0.38(2)	0.3170(3)	0.2080(1)	-0.3099(2)	0.0129(4)
	0.64(2)	0.3155(3)	0.2094(1)	-0.3133(2)	0.0147(5)
	0.0001*	0.3191(4)	0.2059(2)	-0.3045(3)	0.0117(6)
Si5	0.38(2)	0.3325(3)	0.1976(1)	-0.7226(2)	0.0134(4)
	0.64(2)	0.3344(3)	0.1965(1)	-0.7256(2)	0.0156(4)
	0.0001*	0.3297(4)	0.1992(2)	-0.7179(3)	0.0101(6)
O1	0.38(2)	0.250(1)	0	0	0.031(2)
	0.64(2)	0.251(1)	0	0	0.034(2)

	0.0001*	0.249(1)	0	0	0.027(2)
O2	0.38(2)	0.2976(7)	0.5125(3)	0.1748(6)	0.035(1)
	0.64(2)	0.2982(7)	0.5148(3)	0.1749(6)	0.037(1)
	0.0001*	0.2986(8)	0.5111(5)	0.1763(7)	0.034(2)
O3	0.38(2)	0.3968(7)	0.4082(3)	0.0225(5)	0.030(1)
	0.64(2)	0.3977(7)	0.4081(3)	0.0269(5)	0.032(1)
	0.0001*	0.3971(8)	0.4089(4)	0.0175(8)	0.024(2)
O4	0.38(2)	0.3446(7)	0.2199(3)	-0.5131(5)	0.024(1)
	0.64(2)	0.3448(8)	0.2207(3)	-0.5159(5)	0.028(1)
	0.0001*	0.3451(8)	0.2200(3)	-0.5095(7)	0.017(1)
O5	0.38(2)	0.5	0.2886(5)	-0.062(1)	0.030(2)
	0.64(2)	0.5	0.2891(5)	-0.072(1)	0.031(2)
	0.0001*	0.5	0.2893(7)	-0.048(1)	0.025(3)
O6	0.38(2)	0.2370(6)	0.2529(4)	-0.2971(6)	0.039(2)
	0.64(2)	0.2354(7)	0.2547(4)	-0.306(6)	0.040(2)
	0.0001*	0.2412(8)	0.2507(5)	-0.2833(8)	0.031(2)
O7	0.38(2)	0.4008(6)	0.2385(3)	-0.8339(5)	0.021(1)
	0.64(2)	0.4033(7)	0.2366(3)	-0.8369(5)	0.022(1)
	0.0001*	0.3966(7)	0.2408(4)	-0.8300(6)	0.017(2)
O8	0.38(2)	0.3717(7)	0.2614(3)	-0.1796(5)	0.028(1)
	0.64(2)	0.3691(7)	0.2637(3)	-0.1802(5)	0.029(1)
	0.0001*	0.3746(8)	0.2583(4)	-0.1804(7)	0.023(2)
O9	0.38(2)	0.3149(8)	0.0981(3)	-0.2584(5)	0.031(1)
	0.64(2)	0.3138(8)	0.0994(3)	-0.2602(6)	0.034(1)
	0.0001*	0.315(1)	0.0942(4)	-0.2561(7)	0.023(2)
O10	0.38(2)	0.3279(7)	-0.0849(3)	-0.2498(5)	0.026 (1)
	0.64(2)	0.3298(8)	-0.0832(3)	-0.2501(5)	0.028(1)
	0.0001*	0.3249(9)	-0.0873(4)	-0.2477(7)	0.019(2)

$P12_1/n1$

Si1	0.77(3)	0.3485(4)	0.5010(3)	-0.0001(5)	0.0168(6)
	1.13(5)	0.3502(7)	0.5071(3)	-0.0019(7)	0.018(1)
Si21	0.77(3)	0.2736(5)	0.0040(2)	-0.2111(4)	0.0143(8)

	1.13(5)	0.2776(8)	0.0166(4)	-0.2204(6)	0.016(1)
Si22	0.77(3)	0.2729(5)	0.0015(2)	0.2071(4)	0.0153(8)
	1.13(5)	0.2703(9)	0.0151(4)	0.2001(7)	0.019(1)
Si31	0.77(3)	0.4188(6)	0.3014(2)	-0.0183(4)	0.0155(8)
	1.13(5)	0.4189(9)	0.3112(3)	-0.0257(7)	0.016(1)
Si32	0.77(3)	0.4178(6)	-0.2985(2)	0.0151(4)	0.0159(8)
	1.13(5)	0.4170(8)	-0.2907(3)	0.0117(6)	0.013(1)
Si41	0.77(3)	0.3146(5)	0.2130(2)	-0.3156(4)	0.0155(8)
	1.13(5)	0.3101(9)	0.2299(4)	-0.3203(7)	0.024(2)
Si42	0.77(3)	0.3162(6)	-0.2061(2)	0.3133(4)	0.0173(9)
	1.13(5)	0.3177(9)	-0.1881(4)	0.3136(6)	0.017(1)
Si51	0.77(3)	0.3335(6)	0.2001(2)	-0.7273(4)	0.0187(9)
	1.13(5)	0.3316(8)	0.2192(4)	-0.7348(6)	0.019(1)
Si52	0.77(3)	0.3364(6)	-0.1925(2)	0.7253(4)	0.0160(8)
	1.13(5)	0.3454(8)	-0.1751(4)	0.7209(6)	0.018(1)
O1	0.77(3)	0.251(1)	0.0058(8)	-0.003(1)	0.035(2)
	1.13(5)	0.251(2)	0.022(1)	-0.014(1)	0.033(4)
O21	0.77(3)	0.300(1)	0.5144(7)	0.179(1)	0.038(3)
	1.13(5)	0.308(1)	0.518(1)	0.192(2)	0.040(4)
O22	0.77(3)	0.297(1)	-0.5157(7)	-0.170(1)	0.036(3)
	1.13(5)	0.292(1)	-0.5168(8)	-0.160(1)	0.020(3)
O31	0.77(3)	0.399(1)	0.4087(6)	0.024(1)	0.038(3)
	1.13(5)	0.413(1)	0.4245(7)	0.009(2)	0.033(4)
O32	0.77(3)	0.398(1)	-0.4062(6)	-0.032(1)	0.030(2)
	1.13(5)	0.400(2)	-0.3989(7)	-0.047(1)	0.016(3)
O41	0.77(3)	0.342(1)	0.2262(6)	-0.5201(9)	0.028(2)
	1.13(5)	0.334(2)	0.2539(8)	-0.527(1)	0.020(3)
O42	0.77(3)	0.349(1)	-0.2151(6)	0.5129(9)	0.028(2)
	1.13(5)	0.361(2)	-0.1906(8)	0.505(1)	0.026(3)
O5	0.77(3)	0.5006(9)	0.2890(5)	-0.075(1)	0.031(2)
	1.13(5)	0.501(1)	0.293(1)	-0.078(2)	0.033(4)
O61	0.77(3)	0.2351(9)	0.2588(8)	-0.302(1)	0.043(3)
	1.13(5)	0.230(1)	0.277(1)	-0.291(2)	0.036(4)
O62	0.77(3)	0.2360(9)	-0.2522(7)	0.315(1)	0.037(3)
	1.13(5)	0.238(1)	-0.235(1)	0.339(2)	0.031(4)

O71	0.77(3)	0.404(1)	0.2385(6)	-0.8381(9)	0.021(2)
	1.13(5)	0.405(1)	0.2501(9)	-0.842(1)	0.026(4)
O72	0.77(3)	0.406(1)	-0.2332(5)	0.8377(9)	0.020(2)
	1.13(5)	0.414(1)	-0.2181(8)	0.836(1)	0.018(3)
O81	0.77(3)	0.370(1)	0.2670(6)	-0.184(1)	0.028(2)
	1.13(5)	0.369(1)	0.2791(9)	-0.191(2)	0.025(4)
O82	0.77(3)	0.369(1)	-0.2633(6)	0.179(1)	0.030(2)
	1.13(5)	0.367(2)	-0.2522(9)	0.172(2)	0.032(4)
O91	0.77(3)	0.314(1)	0.1028(6)	-0.267(1)	0.037(3)
	1.13(5)	0.312(2)	0.1167(7)	-0.287(2)	0.026(4)
O92	0.77(3)	0.316(1)	-0.0968(5)	0.255(1)	0.030(2)
	1.13(5)	0.321(2)	-0.0801(8)	0.239(2)	0.032(4)
O101	0.77(3)	0.332(1)	-0.0795(6)	-0.250(1)	0.033(3)
	1.13(5)	0.340(1)	-0.0639(7)	-0.245(2)	0.022(3)
O102	0.77(3)	0.329(1)	0.0866(5)	0.251(1)	0.027(2)
	1.13(5)	0.319(2)	0.1048(8)	0.254(2)	0.030(4)

$P2_1/n11$

Si1	1.35(8)	-0.6427(8)	-0.4705(4)	-0.9016(7)	0.0187(6)
	3.00(7)	-0.635(1)	-0.4612(5)	-0.8648(8)	0.0232(7)
Si2a	1.35(8)	-0.6427(8)	-0.4705(4)	-0.9016(7)	0.0187(6)
	3.00(7)	-0.759(1)	-0.4729(5)	-0.5659(8)	0.0232(7)
Si2b	1.35(8)	-0.7852(9)	-0.4818(4)	-0.1833(7)	0.0187(6)
	3.00(7)	-0.787(1)	-0.4766(5)	-0.1423(8)	0.0232(7)
Si3a	1.35(8)	-0.9049(9)	-0.1772(4)	-0.4240(7)	0.0187(6)
	3.00(7)	-0.903(1)	-0.1700(5)	-0.3920(8)	0.0232(7)
Si3b	1.35(8)	-0.5661(9)	-0.2686(4)	-0.9244(7)	0.0187(6)
	3.00(7)	-0.550(1)	-0.2585(4)	-0.8979(8)	0.0232(7)
Si4a	1.35(8)	-0.8302(9)	-0.2758(4)	-0.1115(7)	0.0187(6)
	3.00(7)	-0.831(1)	-0.2679(5)	-0.0722(8)	0.0232(7)
Si4b	1.35(8)	-0.8268(9)	-0.6800(4)	-0.7103(7)	0.0187(6)
	3.00(7)	-0.832(1)	-0.6724(5)	-0.6714(8)	0.0232(7)
Si5a	1.35(8)	-0.800(1)	-0.2740(4)	-0.7059(7)	0.0187(6)
	3.00(7)	-0.793(1)	-0.2642(5)	-0.6629(9)	0.0232(7)

Si5b	1.35(8)	-0.8521(9)	-0.6860(4)	-0.1272(7)	0.0187(6)
	3.00(7)	-0.873(1)	-0.6812(5)	-0.0864(8)	0.0232(7)
O1	1.35(8)	-0.749(2)	-0.4901(9)	-0.390(1)	0.025(1)
	3.00(7)	-0.745(2)	-0.483(1)	-0.344(1)	0.025(1)
O2a	1.35(8)	-0.715(1)	-0.4761(9)	-1.041(2)	0.025(1)
	3.00(7)	-0.711(1)	-0.466(1)	-1.000(2)	0.025(1)
O2b	1.35(8)	-0.680(1)	-0.4751(9)	-0.698(2)	0.025(1)
	3.00(7)	-0.588(2)	-0.3637(9)	-0.908(2)	0.025(1)
O3a	1.35(8)	-0.588(2)	-0.5617(7)	-0.925(2)	0.025(1)
	3.00(7)	-0.577(2)	-0.5546(8)	-0.898(2)	0.025(1)
O3b	1.35(8)	-0.593(2)	-0.3769(8)	-0.926(2)	0.025(1)
	3.00(7)	-0.588(2)	-0.3637(9)	-0.908(2)	0.025(1)
O4a	1.35(8)	-0.843(2)	-0.2551(9)	-0.894(1)	0.025(1)
	3.00(7)	-0.841(2)	-0.241(1)	-0.850(2)	0.025(1)
O4b	1.35(8)	-0.858(2)	-0.7089(8)	-0.908(1)	0.025(1)
	3.00(7)	-0.871(2)	-0.705(1)	-0.868(1)	0.025(1)
O5	1.35(8)	-0.978(1)	-0.2255(9)	-0.523(2)	0.025(1)
	3.00(7)	-0.962(1)	-0.2384(9)	-0.512(2)	0.025(1)
O6a	1.35(8)	-0.753(1)	-0.7396(9)	-0.667(2)	0.025(1)
	3.00(7)	-0.761(1)	-0.745(1)	-0.634(2)	0.025(1)
O6b	1.35(8)	-0.787(1)	-0.749(1)	-0.227(2)	0.025(1)
	3.00(7)	-0.803(1)	-0.747(1)	-0.183(2)	0.025(1)
O7a	1.35(8)	-0.832(1)	-0.2050(9)	-0.543(2)	0.025(1)
	3.00(7)	-0.820(2)	-0.188(1)	-0.496(2)	0.025(1)
O7b	1.35(8)	-0.568(1)	-0.2208(9)	-0.726(1)	0.025(1)
	3.00(7)	-0.545(2)	-0.216(1)	-0.690(2)	0.025(1)
O8a	1.35(8)	-0.896(2)	-0.2144(8)	-0.220(1)	0.025(1)
	3.00(7)	-0.895(2)	-0.120(1)	-0.178(2)	0.025(1)
O8b	1.35(8)	-0.889(1)	-0.7021(9)	-0.5625(16)	0.025(1)
	3.00(7)	-0.898(2)	-0.6809(9)	-0.506(2)	0.025(1)
O9a	1.35(8)	-0.808(2)	-0.5681(7)	-0.6975(15)	0.025(1)
	3.00(7)	-0.807(2)	-0.5602(9)	-0.670(2)	0.025(1)
O9b	1.35(8)	-0.840(2)	-0.3880(7)	-0.1558(15)	0.025(1)
	3.00(7)	-0.847(2)	-0.3830(9)	-0.122(2)	0.025(1)
O10a	1.35(8)	-0.814(2)	-0.3871(7)	-0.6562(15)	0.025(1)

	3.00(7)	-0.808(2)	-0.3757(9)	-0.607(2)	0.025(1)
O10b	1.35(8)	-0.840(2)	-0.5730(7)	-0.1462(15)	0.025(1)
	3.00(7)	-0.846(2)	-0.5685(9)	-0.109(2)	0.025(1)

* Upon decompression

Table 3. The "E" ring-deformation parameters (E = S/L, where S and L are the shortest and longest ring diagonals, respectively) and the O1-O1-O1 intertetrahedral angles (°) (Figure 1), from the four single-crystal experiments using silicone oil, methanol:ethanol:H_2O mixture, ethylene glycol and 2methyl-2propern-1ol PTF, respectively.

Space Group	***P* (GPa)**	**E-10MR[001]**	**E-6MR[001]**	**E-8MR[010]**	**O1-O1-O1**
Pmnn		(O7-O8)/(O7-O8)	(O3-O3)/(O3-O3)	(O7-O8)-(O7-O8)	
$P12_1/n1$		(O72-O82)/(O71-O81)	(O31-O31)/(O32-O32)	(O72-O81)/(O71-O82)	
$P2_1/n11$		(O7b-O8b)/(O7a-O8a)	(O3a-O3a)/(O3b-O3b)	(O7b-O8a)/(O7a-O8b)	
			Silicone oil		
Pmnn	0.38(2)	1	1	1	180
Pmnn	0.52(2)	1	1	1	180
Pmnn	0.64(2)	1	1	1	180
$P12_1/n1$	0.77(3)	0.985(4)	0.979(12)	0.993(6)	179.0(2)
$P12_1/n1$	0.94(3)	0.939(5)	0.876(13)	0.976(8)	176.9(2)
$P12_1/n1$	1.13(5)	0.909(5)	0.819(12)	0.969(8)	175.9(3)
$P2_1/n11$	1.35(8)	0.723(4)	0.768(12)	0.553(5)	169.7(2)
$P2_1/n11$	1.56(4)	0.707(4)	0.752(12)	0.531(5)	168.9(2)
$P2_1/n11$	1.82(5)	0.696(4)	0.728(12)	0.510(5)	168.0(2)
$P2_1/n11$	2.09(7)	0.679(4)	0.723(11)	0.503(5)	167.2(2)
$P2_1/n11$	2.64(9)	0.656(4)	0.709(11)	0.465(5)	165.9(3)
$P2_1/n11$	3.00(7)	0.653(4)	0.684(11)	0.443(5)	165.1(3)
			Methanol:ethanol:H_2O mixture		
Pmnn	0.0001*	1	1	1	180

Pmnn	0.12(2)	1	1	1	180
Pmnn	0.42(2)	1	1	1	180
Pmnn	0.95(2)	1	1	1	180
$P12_1/n1$	1.55(2)	0.943(5)	0.879(11)	0.981(7)	178.82)
$P12_1/n1$	1.97(6)	0.914(5)	0.803(10)	0.956(7)	175.5(2)
$P12_1/n1$	2.56(6)	0.889(5)	0.781(12)	0.952(8)	174.0(2)
$P12_1/n1$	3.24(7)	0.855(6)	0.697(12)	0.947(8)	173.5(2)
$P12_1/n1$	3.86(7)	0.827(6)	0.668(11)	0.947(9)	173.2(2)

Ethylene glycol

Pmnn	0.07(2)	1	1	1	180
Pmnn	0.13(2)	1	1	1	180
Pmnn	0.28(2)	1	1	1	180
Pmnn	0.57(2)	1	1	1	180
$P12_1/n1$	0.93(2)	0.818(4)	0.702(9)	1.000(7)	173.9(2)
$P12_1/n1$	1.39(3)	0.778(4)	0.636(9)	0.999(8)	172.5(2)
$P12_1/n1$	1.77(6)	0.759(5)	0.610(9)	1.000(8)	171.7(2)
$P12_1/n1$	2.37(2)	0.755(5)	0.578(9)	0.991(9)	170.6(2)
Pmnn	0.0001**	1	1	1	180
$P2_1/n11$	1.55(4)**	0.698(3)	0.754(9)	0.518(4)	168.3(2)

2methyl-2propen-1ol

Pmnn	0.15(2)	1	1	1	180
Pmnn	0.27(2)	1	1	1	180
Pmnn	0.42(2)	1	1	1	180
Pmnn	0.58(2)	1	1	1	180
$P12_1/n1$	0.77(3)	0.902(5)	0.832(11)	0.980(10)	176.2(2)
$P12_1/n1$	1.04(5)	0.834(6)	0.703(12)	0.980(11)	174.3(3)
$P12_1/n1$	1.30(3)	0.783(6)	0.631(11)	1.008(10)	172.3(3)
$P12_1/n1$	1.67(2)	0.768(6)	0.610(11)	0.996(11)	171.8(3)

$P12_1/n1$	2.08(4)	0.770(7)	0.575(14)	0.990(13)	171.2(4)
Pmnn	0.0001**	1	1	1	180
$P2_1/n11$	2.00(3)**	0.674(3)	0.741(10)	0.495(4)	167.0(2)

* Upon decompression; ** “Fast compression” experiments (see section 3.2.1 for further details)

Table 4. Unit-cell parameters of Si-FER at different pressures, from the single-crystal experiment using silicone oil as *P*-transmitting fluid.

	P	***a* (Å)**	***b* (Å)**	***c* (Å)**	**α (°)**	**β (°)**	***V* (Å^3)**
P_1	0.38(2)	18.585(5)	14.0126(4)	7.3807(2)			1922.1(5)
P_2	0.52(2)	18.503(5)	13.9893(3)	7.36488(15)			1906.4(5)
P_3	0.64(2)	18.469(5)	13.9729(3)	7.35131(15)			1897.1(5)
P_4	0.77(3)	18.422(6)	13.9566(3)	7.33913(18)		90.056(5)	1887.0(5)
P_5	0.94(3)	18.319(10)	13.9396(6)	7.3276(3)		90.148(5)	1871.2(4)
P_6	1.13(5)	18.215(11)	13.9002(6)	7.3032(3)		90.201(8)	1849.2(4)
P_7	1.35(8)	17.64(2)	13.8224(12)	7.2685(7)	91.308(6)		1772.2(6)
P_8	1.56(4)	17.52(2)	13.7828(11)	7.2418(7)	91.457(6)		1747.9(6)
P_9	1.82(5)	17.315(18)	13.7501(9)	7.2245(6)	91.669(5)		1719.6(3)
P_{10}	2.09(7)	17.14(2)	13.7151(11)	7.2042(7)	91.874(6)		1693.1(6)
P_{11}	2.64(9)	16.75(2)	13.6583(12)	7.1707(7)	92.201(6)		1639.2(6)
P_{12}	3.00(7)	16.59(2)	13.6020(12)	7.1373(7)	92.381(6)		1609.1(6)
P_{REV}	0.0001	18.718(8)	14.0678(4)	7.4148(2)			1952.5(8)

* Upon decompression;

P_1-P_3, P_{REV}: *Pmnn*-polymorph; P_4-P_6: $P12_1/n1$ polymorph; P_7-P_{12}: $P2_1/n11$ polymorph

Figure captions

Figure 1. (*Top*) A view down to the **c**-axis of the 10- and 6-membered rings of tetrahedra of the [FER] framework. (*Center*). A view down to the **b**-axis of the 8-membered ring of tetrahedra of the [FER] framework. The ring diagonals, reported in Table 3, are shown, along with a reproduction of the mirror plane at $x = 0$ in the *Pmnn*-polymorph. (*Bottom*). The tetrahedral framework of the $P12_1/n1$-polymorph of Si-FER viewed down the [001] crystallographic axis. The intertetrahedral O1-O1-O1 angle is shown.

Figure 2. Synchrotron X-ray powder patterns of Si-FER collected at different pressures from the H*P*-experiments in ethylene glycol (*left*) and 2methyl-2propen-1ol (*right*).

Figure 3. *P*-induced evolution of the unit-cell volume (A) and of the unit-cell edges (B, C and D) of Si-FER, based on the single-crystal experiment in silicone oil.

Figure 4. Reconstruction of selected reciprocal lattice planes of the *Pmnn*-, $P12_1/n1$- and $P2_1/n11$-polymorphs of Si-FER, based on the single-crystal experiment using silicone oil as *P*-transmitting fluid.

Figure 5. The *P*-induced evolution of the unit-cell volumes of Si-FER, based on the single-crystal and powder diffraction experiments using methanol:ethanol:H_2O mixture (*top*), ethylene glycol (*center*) and 2methyl-2propen-1ol (*bottom*) as *P*-transmitting fluids.

Figure 6. Sections at $z = 0$ ($0.2 \leq x \leq 1.4$; $0.5 \leq y \leq 1.5$) of the difference-Fourier maps of the electron density calculated from the following single-crystal data: A) *Pmnn*-

polymorph, m.e.w. experiment [0.95(2) GPa]; B) $P12_1/n1$-polymorph, m.e.w. experiment [2.56(6) GPa)]; C) $P12_1/n1$-polymorph, e.gl. experiment [1.77(6) GPa]; D) $P12_1/n1$-polymorph, m.p.o. experiment [1.30(3) GPa]. The disordered distribution of the residual peaks at the center of the *fer*-cage and within the 10-ring channels can be observed.

Figure 7. *P*-induced evolution of the unit-cell volumes of the *Pmnn*- (*left*) and the $P12_1/n1$-polymorphs (*right*) of Si-FER, based on single-crystal experiments with the four different *P*-fluids.

Figure 8. The "E" deformation parameters (E = S/L, where S and L are the shortest and longest ring diagonals, respectively) of the 10- (A), 6- (B) and 8-membered (C) rings of tetrahedra, as a function of pressure, and the *P*-induced evolution of the O1-O1-O1 intertetrahedral angle (D). Data based on single-crystal experiments with the four different *P*-fluids.

Figure 1

Click here to download high resolution image

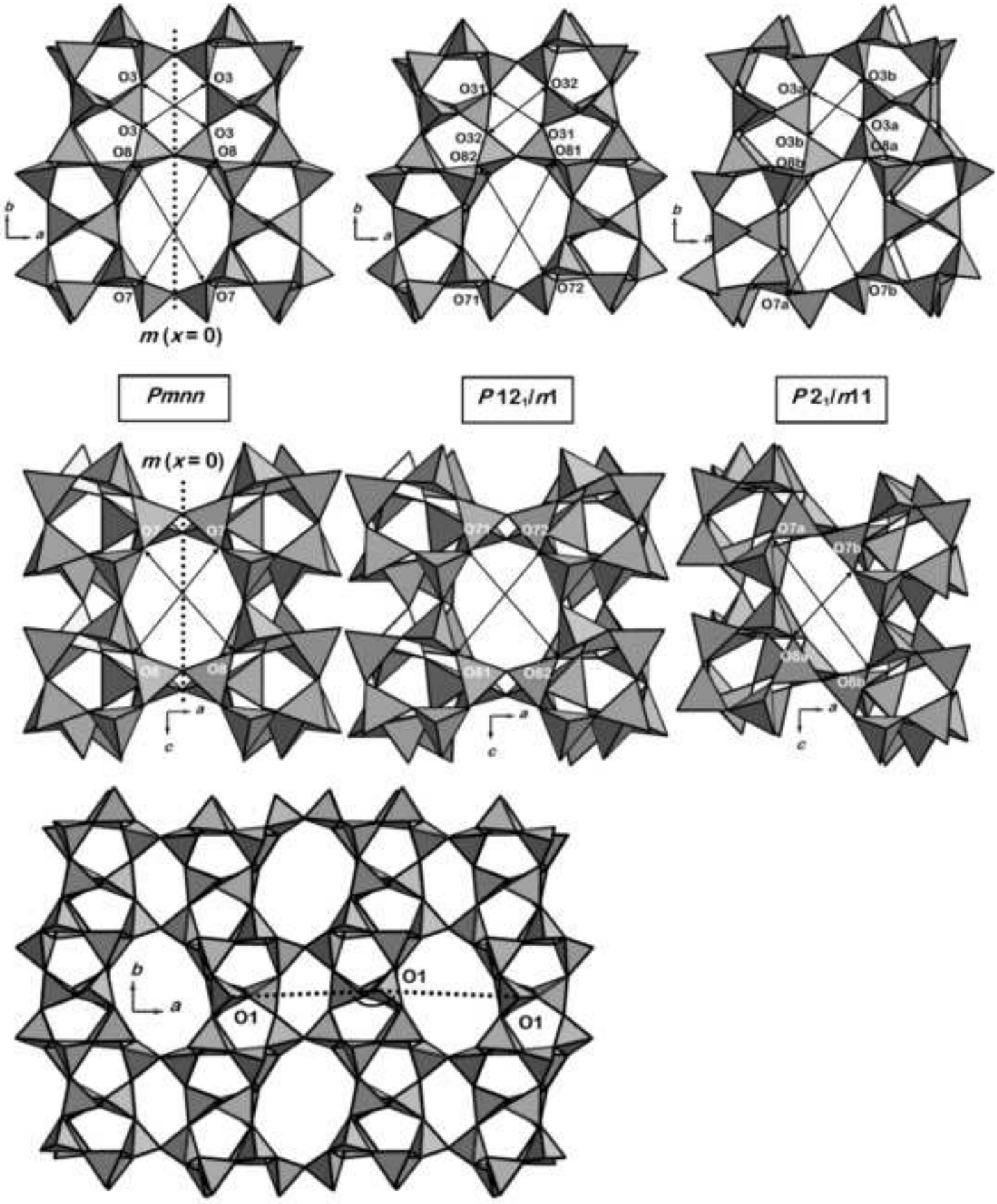

Figure 2

Click here to download high resolution image

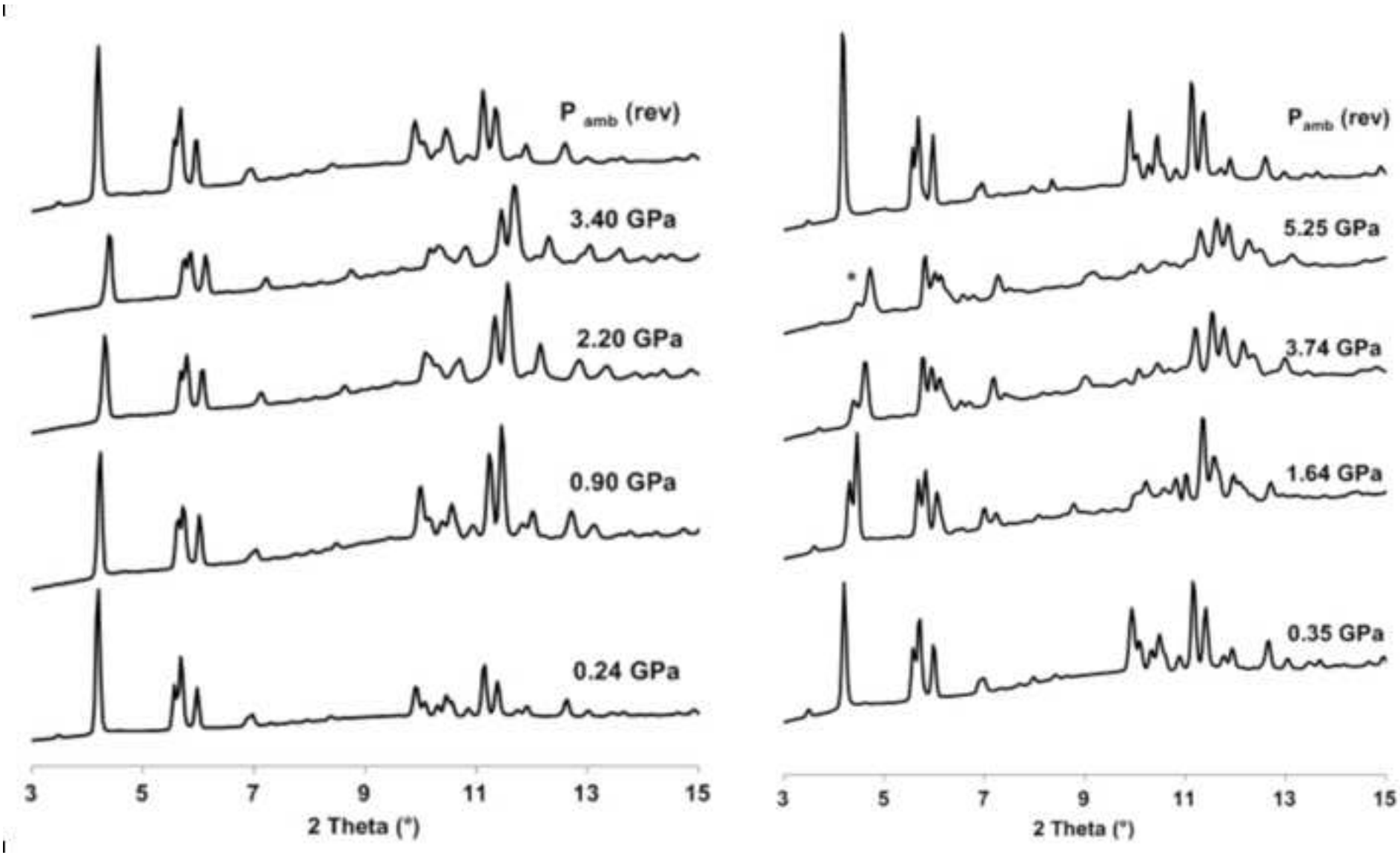

Figure 3

Click here to download high resolution image

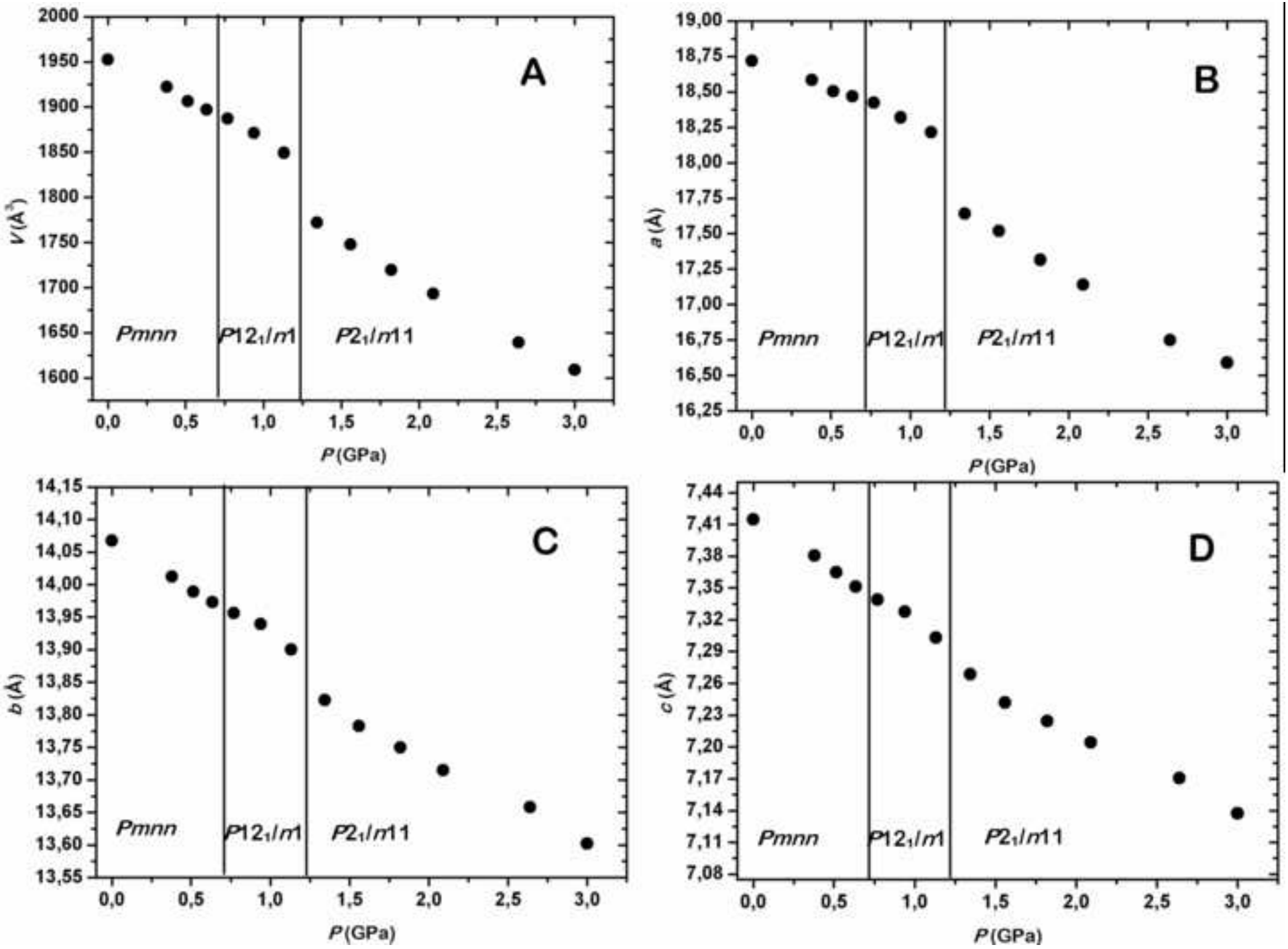

Figure 4

Click here to download high resolution image

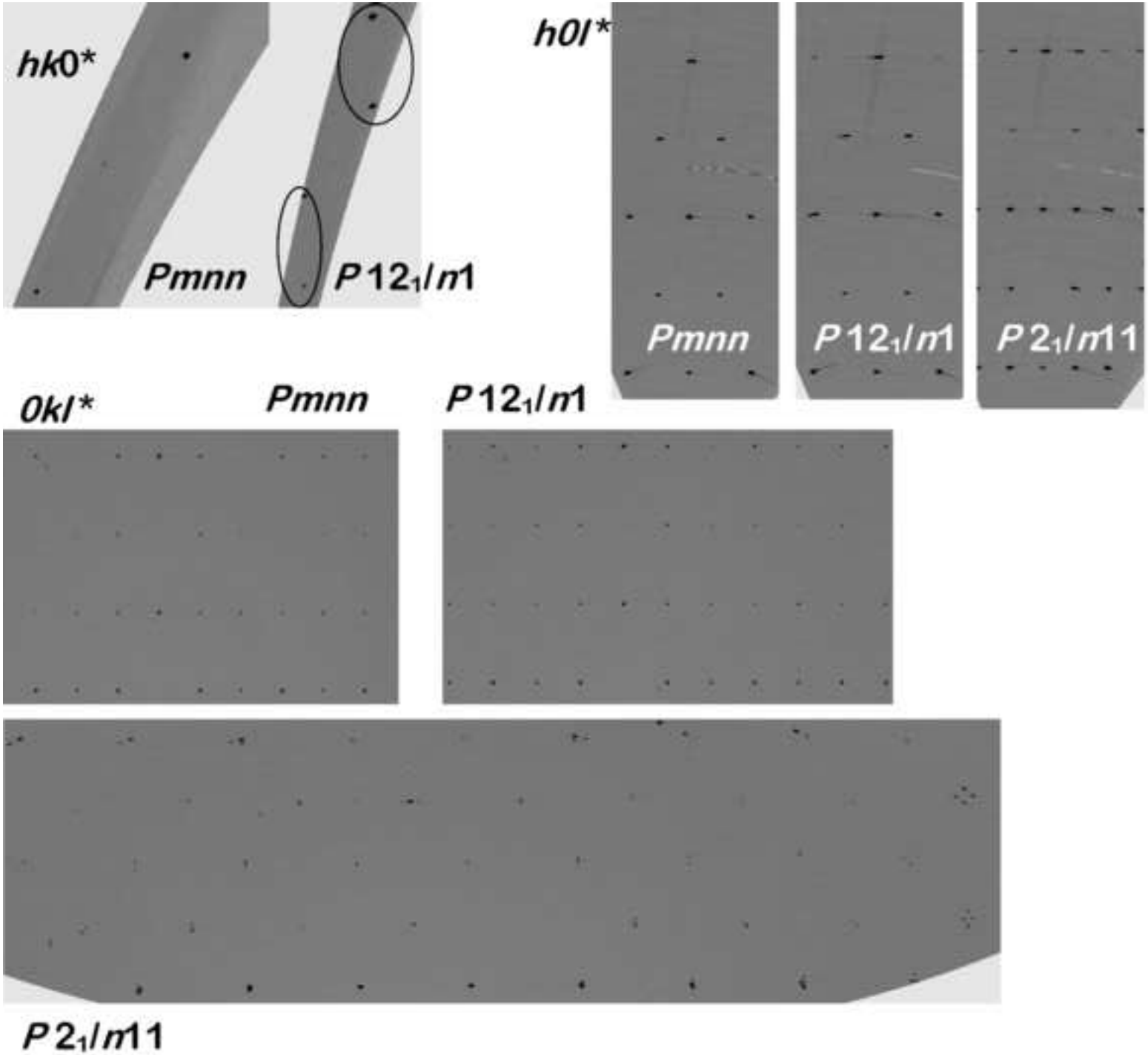

Figure 5

Click here to download high resolution image

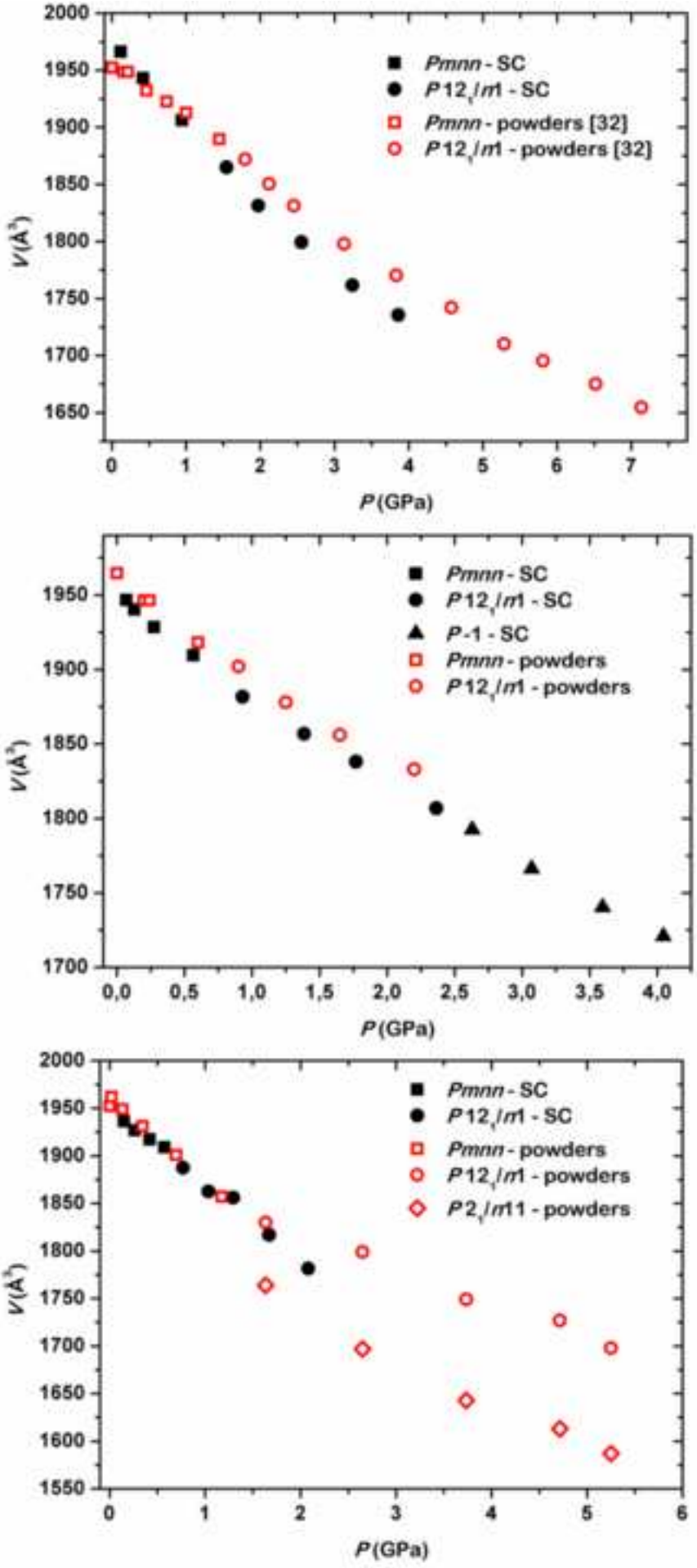

Figure 6

Click here to download high resolution image

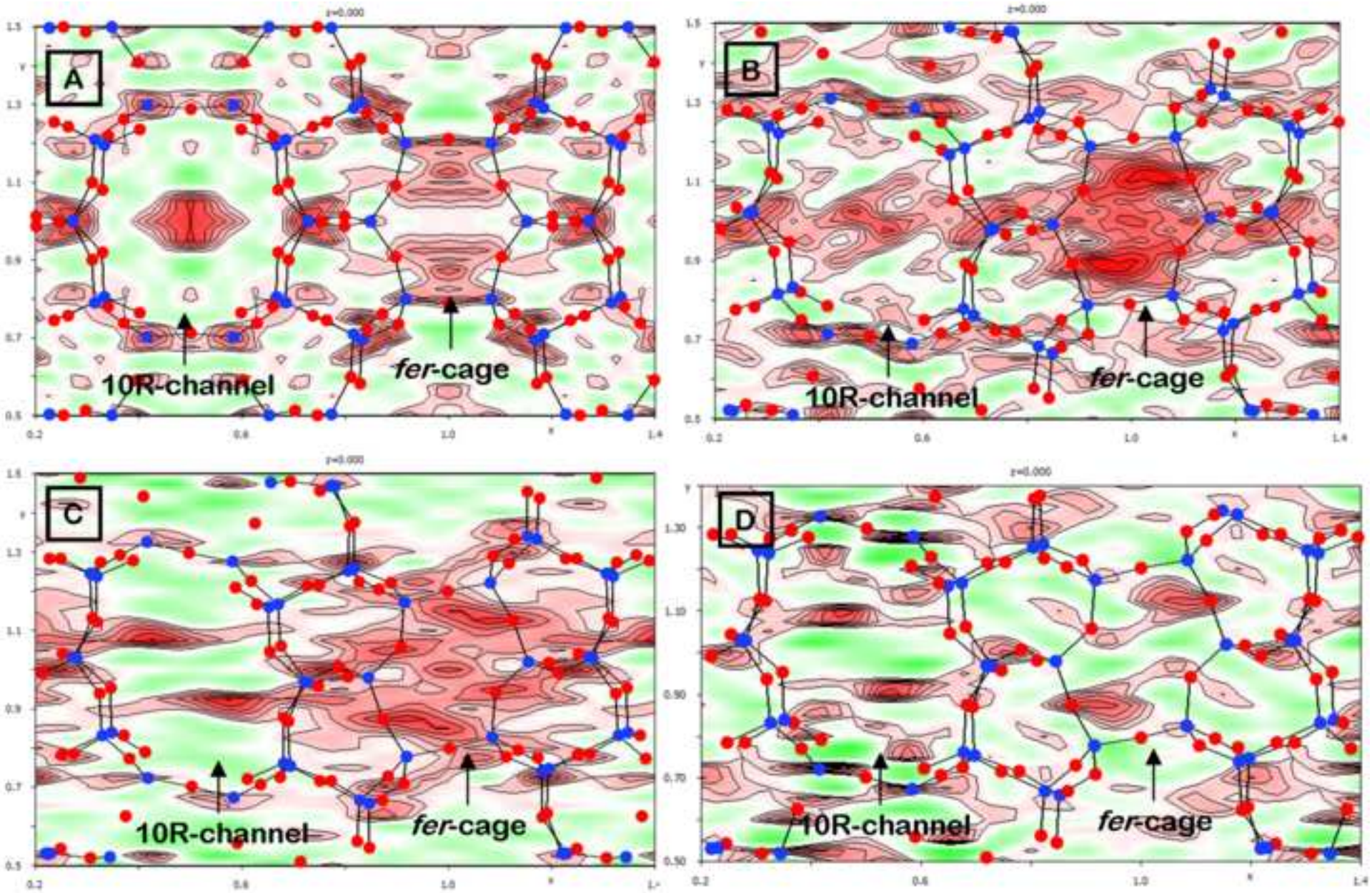

Figure 7

Click here to download high resolution image

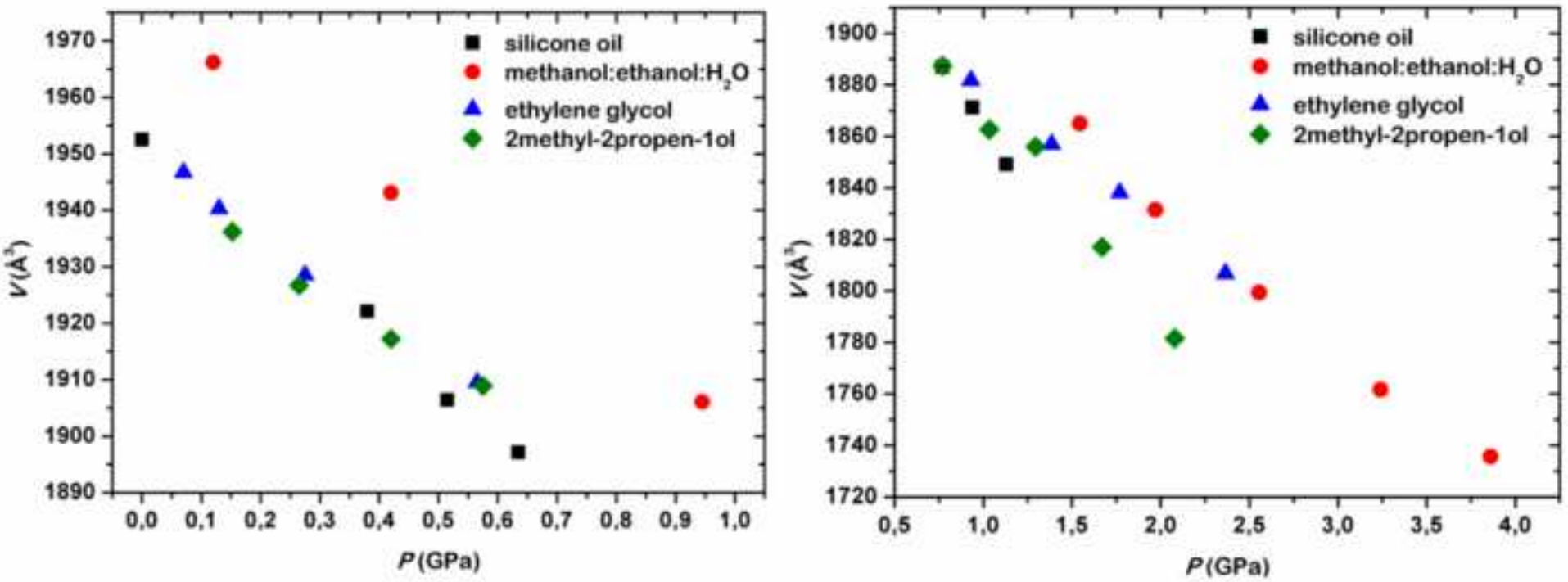

Figure 8

Click here to download high resolution image